AMERICAN SOCIETY FOR MICROBIOLOGY | Microbiology Spectrum

RESEARCH ARTICLE

Structural and Functional Analysis of SsaV Cytoplasmic Domain and Variable Linker States in the Context of the InvA-SsaV Chimeric Protein

Jinghua Xu,[a] Jiuqing Wang,[a] Aijun Liu,[b] Yanqing Zhang,[b] Xiang Gao[a,c]

[a]State Key Laboratory of Microbial Technology, Shandong University, Qingdao, China
[b]Shanghai Fifth People's Hospital and Shanghai Key Laboratory of Medical Epigenetics, International Co-laboratory of Medical Epigenetics and Metabolism (Ministry of Science and Technology), Institutes of Biomedical Sciences, Fudan University, Shanghai, China
[c]School of Life Sciences, Shandong University, Qingdao, China

ABSTRACT The type III secretion (T3S) injectisome is a syringe-like protein-delivery nanomachine widely utilized by Gram-negative bacteria. It can deliver effector proteins directly from bacteria into eukaryotic host cells, which is crucial for the bacterial–host interaction. Intracellular pathogen *Salmonella enterica* serovar Typhimurium encodes two sets of T3S injectisomes from *Salmonella* pathogenicity islands 1 and 2 (SPI-1 and SPI-2), which are critical for its host invasion and intracellular survival, respectively. The inner membrane export gate protein, SctV (InvA in SPI-1 and SsaV in SPI-2), is the largest component of the injectisome and is essential for assembly and function of T3SS. Here, we report the 2.11 Å cryo-EM structure of the SsaV cytoplasmic domain ($SsaV_C$) in the context of a full-length SctV chimera consisting of the transmembrane region of InvA, the linker of SsaV ($SsaV_L$) and $SsaV_C$. The structural analysis shows that $SsaV_C$ exists in a semi-open state and $SsaV_L$ exhibits two major orientations, implying a highly dynamic process of SsaV for the substrate selection and secretion in a full-length context. A biochemical assay indicates that $SsaV_L$ plays an essential role in maintaining the nonameric state of SsaV. This study offers near atomic-level insights into how $SsaV_C$ and $SsaV_L$ facilitate the assembly and function of SsaV and may lead to the development of potential anti-virulence therapeutics against T3SS-mediated bacterial infection.

IMPORTANCE Type III secretion system (T3SS) is a multicomponent nanomachine and a critical virulence factor for a wide range of Gram-negative bacterial pathogens. It can deliver numbers of effectors into the host cell to facilitate the bacterial host infection. Export gate protein SctV, as one of the engines of T3SS, is at the center of T3SS assembly and function. In this study, we show the high-resolution atomic structure of the cytosolic domain of SctV in the nonameric state with variable linker conformations. Our first observation of conformational changes of the linker region of SctV and the semi-open state of the cytosolic domain of SctV in the full-length context further support that the substrate selection and secretion process of SctV is highly dynamic. These findings have important implications for the development of therapeutic strategies targeting SctV to combat T3SS-mediated bacterial infection.

KEYWORDS *Salmonella*, type III secretion system, injectisome, export gate protein, cryo-EM

The type III secretion system (T3SS) is a supramolecular nanomachine employed by numerous Gram-negative bacteria to facilitate pathogenic or symbiotic interactions between microbes and their eukaryotic hosts (1, 2). The T3SS, an ~3.5 MDa protein complex consisting of more than 20 proteins, possesses two types of bacterial

Editor Cezar M. Khursigara, University of Guelph

Address correspondence to Xiang Gao, xgao@email.sdu.edu.cn, or Yanqing Zhang, zyq_lab@fudan.edu.cn.

Received 10 August 2021
Accepted 5 November 2021
Published 1 December 2021

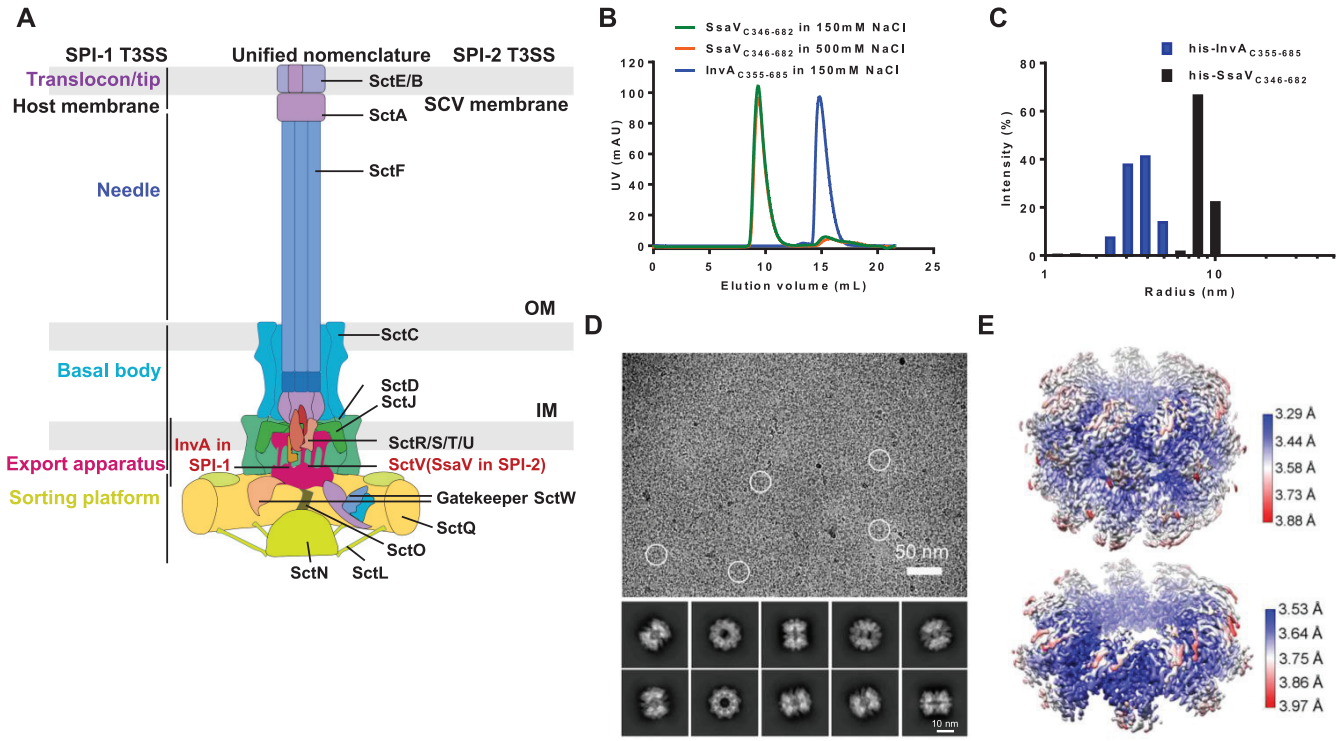

FIG 1 $SsaV_C$ tends to be a stable nonamer compared with $InvA_C$ in solution. (A) Cartoon representation of T3SS injectosome in SPI-1 and SPI-2. SctV is shown in red. (B) Gel filtration traces of purified $InvA_C$ and $SsaV_C$ in two different salt concentrations. $InvA_C$ elutes as a monomer while $SsaV_C$ elutes as a nonamer under physiological and high salt conditions. (C) Oligomeric states of $SsaV_C$ and $InvA_C$ measured by Dynamic Light Scattering (DLS). (D) Representative micrograph and 2D class averages of $SsaV_C$. Representative particles in the micrograph are highlighted with white circles (top panel). Double layer features of the $SsaV_C$ are obvious in the 2D class averages (bottom panel). (E) Local resolution map of $SsaV_C$ with D9 symmetry with an average resolution at 3.55 Å resolution (top panel) and C9 symmetry with an average resolution at 3.64 Å resolution (bottom panel). The local resolution maps were presented with UCSF Chimera.

molecular machines, the flagellum and injectisome, with highly conserved architectures but different functions (3–5). The flagellum is a crucial apparatus involved in bacterial motility (6). The injectisome sits in the bacterial envelope and spans three biological membranes: the inner and outer membranes of the bacteria, and the membrane of host cells. This structure thus bridges individuals from two kingdoms with a hollow conduit, through which bacterial effectors can be directly delivered into eukaryotic host cells and modulate hosts' physiological functions (1, 7–9). Type III secretion (T3S) injectisome comprises several protein complexes, including the sorting platform, export apparatus, basal body, needle, and translocon (10–12). Each complex is made up of one or more proteins. The well-organized assembly and effective cooperation of these complexes ensure that the T3S injectisome can inject effectors from bacteria into the host cells with precise regulation (12–14).

The intracellular bacterial human pathogen *Salmonella enterica* serovar Typhimurium possesses two sets of T3S injectisome, which are encoded in *Salmonella* pathogenicity islands 1 and 2 (SPI-1 and SPI-2) (15, 16). SPI-1 T3SS is activated and assembled in extracellular bacteria and primarily facilitates the invasion of host cells (17, 18). After entry into host cells, the bacteria form a *Salmonella*-containing vacuole (SCV), then utilize the SPI-2 T3SS to mediate host cell signaling in order to promote its own growth, replication, and further dissemination in host tissues (19–23). Although the functions of effectors secreted by SPI-1 and SPI-2 T3SSs are largely different, most of the building blocks are highly conserved between the two systems, both in structure and function (Fig. 1A).

The export gate protein SctV (InvA in SPI-1 and SsaV in SPI-2), located at the outermost layer of the export apparatus, is the largest and the first identified component of the *Salmonella* T3S injectisome (12, 24). SctV comprises a highly conserved N-terminal transmembrane (TM) domain and a less conserved C-terminal cytoplasmic domain

($SctV_C$), which are connected via a ~20–40 amino acid linker, $SctV_L$, in most bacteria using the T3SS (12). It has been reported that SctV is one of the "engines" of T3SS (25); the TM domain forms a putative proton channel, and $SctV_C$ forms a nonameric ring connecting to SctN (ATPase) through SctO (the stalk protein) to function as the F_0F_1-ATPase, coupling energy from ATP hydrolysis and the proton-motive force to secrete unfolded bacterial effectors into the eukaryotic host (26–29). $SctV_C$ is also involved in substrate selection through recognizing gatekeeper proteins or different effector-chaperone pairs (15, 30–34). A previous study showed that substituting homologous TM and cytoplasmic domains between some SctV proteins caused them to retain their functions, but that $SctV_C$ controls substrate specificity (35).

Intensive structural and functional studies of T3SS have uncovered much detailed structural information and potential assembly processes of this complicated molecular machine (12, 36–40). However, the structure and molecular mechanism of SctV are mostly unknown due to the challenges of obtaining the fully assembled state of the full-length protein. Several studies have isolated the entire T3S injectisome and flagellar basal body for structural studies (12, 41–43). However, SctV was missing in all these trials, even though all other export apparatus components could be captured; this suggests a loose interaction between SctV and other components of the export apparatus and the basal body. The structure of $SctV_C$ has been identified as a homo-nonamer through crystal and cryo-electron microscopy (cryo-EM) structural studies, and the intermolecular polar interactions between monomers are thought to be the leading force maintaining the $SctV_C$ oligomeric state (26, 44–46). Recently, an *in situ* cryo-electron tomography (cryo-ET) study identified the location of InvA in the bacterial inner membrane and showed a high-order oligomeric state of the TM domain of InvA (12). More recently, Matthews-Palmer et al. and Kuhlen et al. obtained assembled full-length SctV and FlhA suitable for cryo-EM structural studies (47, 48). However, due to the structural flexibility issues, both groups only determined the structure of $SctV_C$ and $FlhA_C$, leaving the structure of linker region and the TM domain still unknown.

In this study, through generating a chimeric protein consisting of the TM region of InvA and the cytoplasmic region of SsaV, we produced the full-length SctV in a high-order oligomeric state which was adequate for structural study using cryo-EM single particle analysis. Here, we present the 2.11 Å nonameric ring structure of $SsaV_C$ with a semi-open state of each monomer. Moreover, we display the cryo-EM structure of $SsaV_L$ through the single particle analysis for the first time although with low resolution. Interestingly, $SsaV_L$ exhibits two major orientations, consistent with previous reports that the conformations of the SctV linker region could be altered during the secretion cycle (49, 50). Structural analysis and biochemical assays indicate that $SsaV_L$ plays an essential role in maintaining the nonameric state of SsaV. Collectively, our data provide an atomic view and mechanistic understanding of how the cytoplasmic domain and linker region of SctV facilitate its assembly and function.

RESULTS

$SsaV_C$ forms a stable homo-nonameric ring. To determine the structure of SctV, we initially tried to purify the full-length InvA protein from *Salmonella* SPI-1 T3SS. However, we were unable to obtain a stably-assembled InvA sample for the cryo-EM structural study, even after several rounds of high-throughput detergent screening. It has been shown that $SctV_C$ makes a significant contribution in maintaining the SctV nonamer (46). Previous structural studies suggested that $InvA_C$ tends to be a monomer in solution (51). Therefore, it may be challenging for the full-length InvA to form the stable nonamer outside of the membrane. To obtain a fully assembled SctV sample, we first tested the nonamerization ability of $SsaV_C$, the homologous protein of $InvA_C$ from *Salmonella* SPI-2 T3SS. Unlike $InvA_C$, $SsaV_C$ could maintain a very stable high oligomeric state even in the high salt concentration analyzed by the size exclusion chromatography (SEC; Fig. 1B) and dynamic light scattering (DLS; Fig. 1C). Through a cryo-EM single particle analysis approach, we reconstructed and classified two conformations of

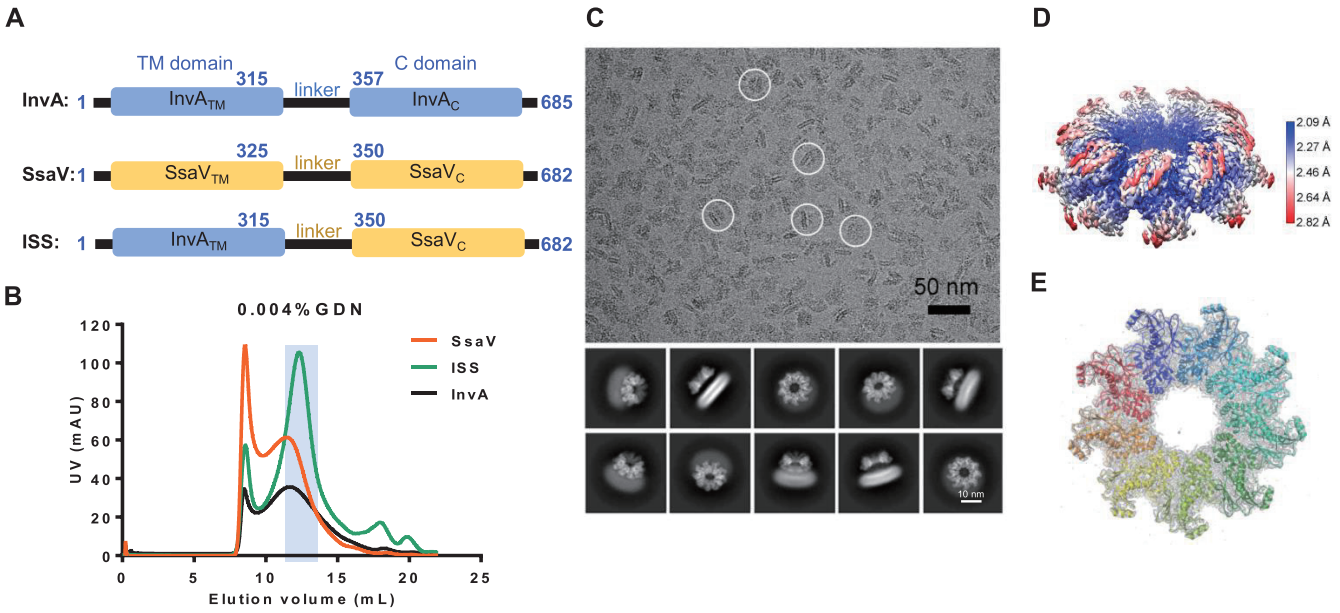

FIG 2 $InvA_{TM}$-$SsaV_C$ chimera (ISS) forms a nonamer in GDN micelles. (A) A diagram for the chimera design. Residues 316–685 of InvA are replaced by residues 326–682 of SsaV. (B) Final SEC purification of the chimeric ISS, InvA and SsaV full-length protein in 0.004% GDN. The main peak fractions of the chimeric ISS (highlighted in the light blue background) are used for cryo-EM analysis. (C) Representative micrograph and 2D class averages of the chimeric ISS. Characteristic particles in distinct orientations are highlighted by white circles (top panel). TM region of the chimeric ISS is visible clearly in 2D class averages (bottom panel). (D) The local resolution map of the chimeric ISS is at 2.11 Å resolution, while the high-resolution part is $SsaV_C$. The TM and linker regions are hardly visible at this resolution because of structural flexibility. The local resolution maps were presented with UCSF Chimera. (E) The atomic model of $SsaV_C$ in rainbow fitted into its EM-map in gray.

$SsaV_C$: one 3.55 Å cryo-EM structure with double stacked nonameric rings with D9 symmetry, and the other 3.64 Å cryo-EM structure with a single nonameric ring with C9 symmetry, the particle number of which are approximately comparable (Fig. 1D and E and Fig. S1 in the supplemental material). The double-layer ring conformation of $SsaV_C$ is considered to be an artifact, consistent with a previous study (45). Notably, most of the C9 single-layer ring of the $SsaV_C$ particles were calculated from top views, and most of the D9 double-layer ring of $SsaV_C$ particles came from side views. We speculate that this is because the top-view protein particles are more vulnerable to air–water interface damage than the side-view particles (52). Together, unlike $InvA_C$, $SsaV_C$ could form the stable homo-nonameric ring in solution.

$InvA_{TM}$-$SsaV_C$ chimeric full-length protein can assemble into a nonamer. To test if the full-length SsaV and the TM domain of InvA could form the stable nonamer in solution with $SsaV_C$, we constructed the full-length SsaV protein and the chimeric full-length protein $InvA_{TM}$-$SsaV_L$-$SsaV_C$ (ISS; Fig. 2A). We performed a high-throughput detergent screening to identify suitable detergents to help stabilize the assembled state of SsaV and ISS. However, very few detergents could generate protein samples of high enough quality for cryo-EM structural study. A homogeneous and oligomerized ISS protein was eventually obtained in buffer containing the detergent Glyco-diosgenin (GDN; Fig. 2B); however, SsaV (similarly to InvA) could not form the stable nonamer in this condition (Fig. 2B). Compared with full-length SsaV and InvA, GDN-solubilized ISS protein showed better SEC and cryo-EM micrograph behaviors (Fig. 2B and C) and were suitable for cryo-EM data processing.

Further 2D classification and 3D reconstruction of ISS showed the apparent density of the $SsaV_C$ nonameric ring, which is consistent with structural features of the $SsaV_C$ domain described above (Fig. 2C and D and Fig. S2). We reconstructed a high-resolution cryo-EM structure of $SsaV_C$ with an averaged resolution of 2.11 Å (Fig. 2D and Fig. S2). Unlike $SsaV_C$, for which we obtained high-resolution structural information, the EM density of $InvA_{TM}$ is blurry, and the $SsaV_L$ EM density is absent, with an approximately constant distance between the cytoplasmic domain and TM domain; this is

consistent with a recent study (47). In summary, we found that the GDN-solubilized $InvA_{TM}$-$SsaV_C$ chimeric full-length protein tended to assemble into a nonamer in solution.

Structure of $SsaV_C$. Based on the 2.11 Å cryo-EM map of ISS solved above (Fig. 2D and Fig. S2), we built an atomic model of the $SsaV_C$ nonamer by referring to the $SsaV_C$ monomer structure (PDB: 7AWA) solved recently (47) (Fig. 2E, Fig. 3A, Fig. S3, and Table S1 in the supplemental material). The high structural similarity between these two $SsaV_C$ monomer structures (Cα RMSDs: 1.3598 Å) indicates that they hold a consistent structural conformation in the context of different TM regions (Fig. S4). Consistent with other reported $SctV_C$ structures (26, 44, 45, 47, 50, 53), the $SsaV_C$ monomer also has a four-subdomain (SD) structure and further assembles to a nonameric ring aligned to SD3, which is the most conserved region of $SsaV_C$ (Fig. 3A to D). The diameter of the channel at the center of the $SsaV_C$ nonamer ranges from ~54-41 Å from the cytosolic face to the TM face (Fig. 3D). This channel further connects to the channel formed by other components of the export apparatus (SctRST) and finally extends to the needle conduit with a diameter of ~25 Å (54). Through this reverse funnel-like channel, T3SS systematically unfolds effector proteins and secretes them out of the bacteria. During the effector secretion process, $SsaV_C$ was reported to involve substrate selection with the cleft between SD2 and SD4 (13, 32). The dynamic conformations between SD2 and SD4 have been demonstrated through both different $SsaV_C$ structures and molecular dynamic simulation, showing that SD2 and SD4 can alternate between open and closed states hinging around the rigid SD3 (13, 26, 44, 45, 47).

Consistent with the observation above, B-factor analysis of the $SsaV_C$ structure also shows that SD3 is the most stable region of $SsaV_C$ with the more flexible SD2 and SD4 floating around it (Fig. 3E). Structural comparison between $SsaV_C$ and $InvA_C$ (51) in a closed conformation or its counterpart in flagellum, $FlhA_C$ (55), in an open conformation shows that $SsaV_C$ in a full-length context presents a semi-open conformation (Fig. 3F and G). Recent structural study revealed that the $YscV_C$ (the homolog of SsaV from *Yersinia enterocolitica*) and $FlhA_C$ in a full-length context present in the open state (48). Comparison of our $SsaV_C$ structure with these two reported homologous structures also exhibits the different conformations between SD2 and SD4 (Fig. S5 in the supplemental material). Together, these findings firstly show the dynamic conformations between SD2 and SD4 of SctV in a full-length context.

The essential roles of linker region for the structural stability and function of SsaV. To gain insights into the molecular mechanism of $SsaV_C$ nonamerization, we analyzed the electrostatic surface potential of the interfaces between $SsaV_C$ monomers within the nonamer and found that electrostatic interactions in SD3 and SD1 of $SsaV_C$ may facilitate the subunit nonamerization (Fig. 4A). Close inspection of the oligomerization interfaces revealed that four pairs of salt bridges presenting in SD3-SD3 (R534-E488, E502-R490) and SD3-SD1 (R567-E407, R563-E482) could stabilize the $SsaV_C$ nonamer (Fig. 4B and Fig. S6A), which is consistent with the electrostatic surface potential analysis above and with previous studies (26, 44, 45, 47). $SctV_L$ has also been reported to be required for forming the $SctV_C$ ring (45, 50). In each $SsaV_C$ monomer, the hydrophobic pocket at the connection region between SD1 and SD3 is occupied by a hydrophobic peptide (M346-V347-P348-G349-A350) from the neighboring $SsaV_L$, forming the hydrophobic interactions between two adjacent subunits (Fig. 4C and Fig. S6B). To verify the importance of these two different intermolecular interactions for the $SsaV_C$ nonameric structure formation, we created two variants, $SsaV_C$M4 (E407A, E482A, E488A, R490A) and $SsaV_C$N4 (deletion of M346-V347-P348-G349), and tested the oligomerization ability of these two variants through SEC. The results showed that neither variant could oligomerize in solution (Fig. 4D), indicating that both intermolecular salt bridges and hydrophobic interactions are essential for $SsaV_C$ nonamerization.

The intermolecular salt bridges are remarkably conserved in all reported $SsaV_C$ structures, consistent with a general role in maintaining the $SctV_C$ ring structure (26, 44, 45, 47). The hydrophobic pocket at the connection region of the SD1 and SD3 is also exhibited in $SsaV_C$ homologous proteins $InvA_C$, $CdsV_C$, $EscV_C$, $MxiA_C$ and $FlhA_C$ (Fig. 4E). However, the hydrophobicity of the pocket-nested peptide from the

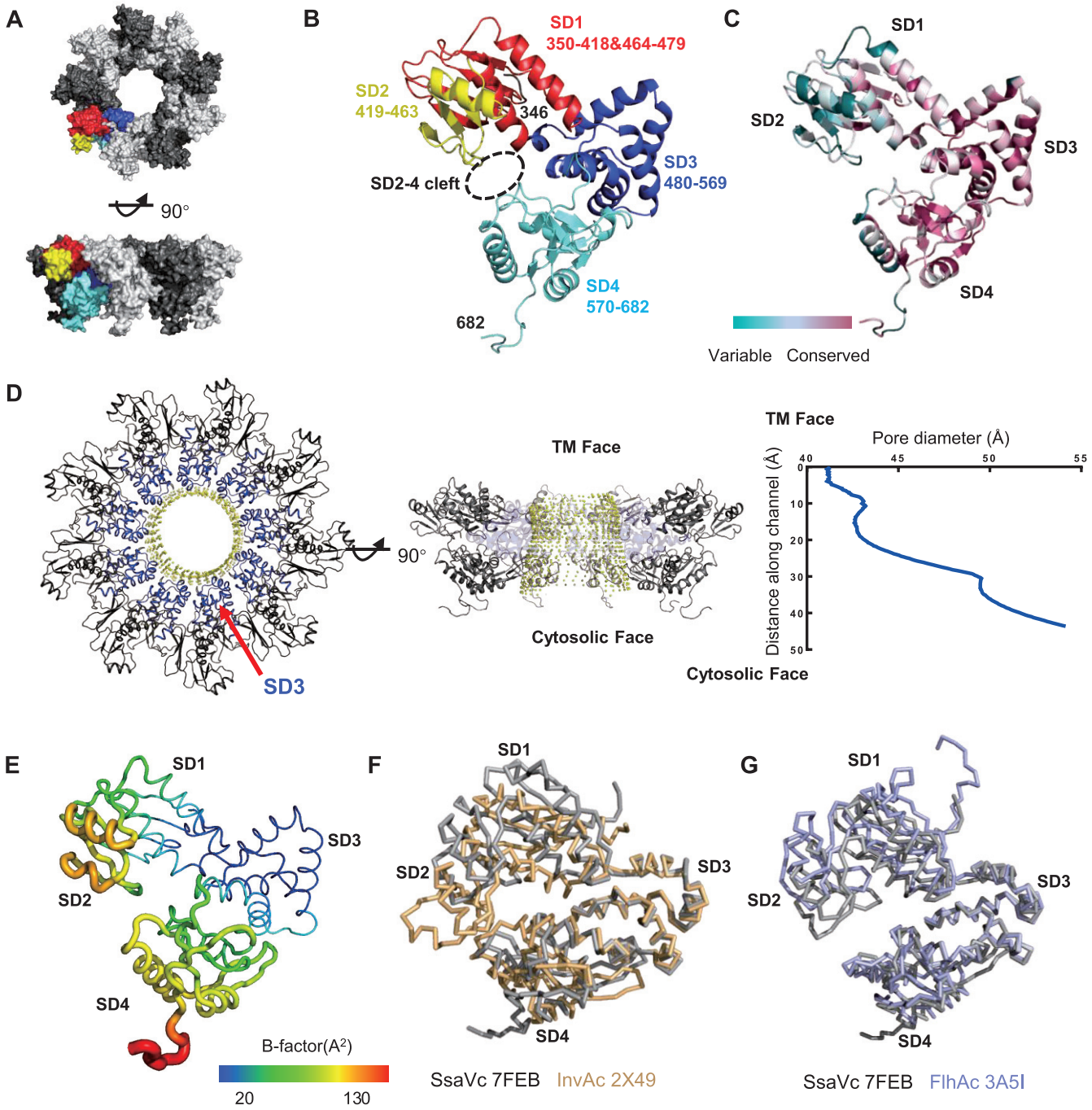

FIG 3 Structure analysis of $SsaV_C$. (A) Surface representation of $SsaV_C$ nonamer, top and side views. The colored monomer corresponds to $SsaV_C$ monomer. (B) The $SsaV_C$ monomer with SD1 (residues 350–418, 464-479) in red; SD2 (residues 419–463) in yellow; SD3 (residues 480–569) in blue; SD4 (residues 570–682) in cyan. The dotted circle in black represents a cleft between SD2 and SD4. (C) Sequence conservation of $SsaV_C$ colored according to residue identity conservation scores obtained by ConSurf. These amino acid sequences are from 16 members of the SctV family. (D) Diameters of the channels at the center of $SsaV_C$ nonamer. The channels illustrated by yellow dots are mainly surrounded by SD3 shown in blue in top view (left panel). Side view of the channels in $SsaV_C$ nonamer (middle panel). The pore diameter diagram calculated using the Hole program in Coot (right panel). (E) Cartoon representation of $SsaV_C$ monomer colored according to B-factor values. (F-G) Overlay of SD3 of $SsaV_C$ monomer in gray with $InvA_C$ in a closed state (wheat, PDB:2X49) and $FlhA_C$ in an open state (purple, PDB:3A5I). The $SsaV_C$ monomer is shown in a semi-open conformation.

neighboring $SctV_L$ exhibits great diversity in different homologous proteins (Fig. 4F). $InvA_C$, $EscV_C$ and $FlhA_C$ show relative hydrophobic pockets at the connection region of the SD1 and SD3. However, the interaction peptide from $InvA_L$ (VSTET) is very hydrophilic, and those from $EscV_L$ (ISPGA) and $FlhA_L$ (SLGME) are less hydrophobic than $SsaV_L$, reducing the hydrophobic interactions between neighboring subunits. The

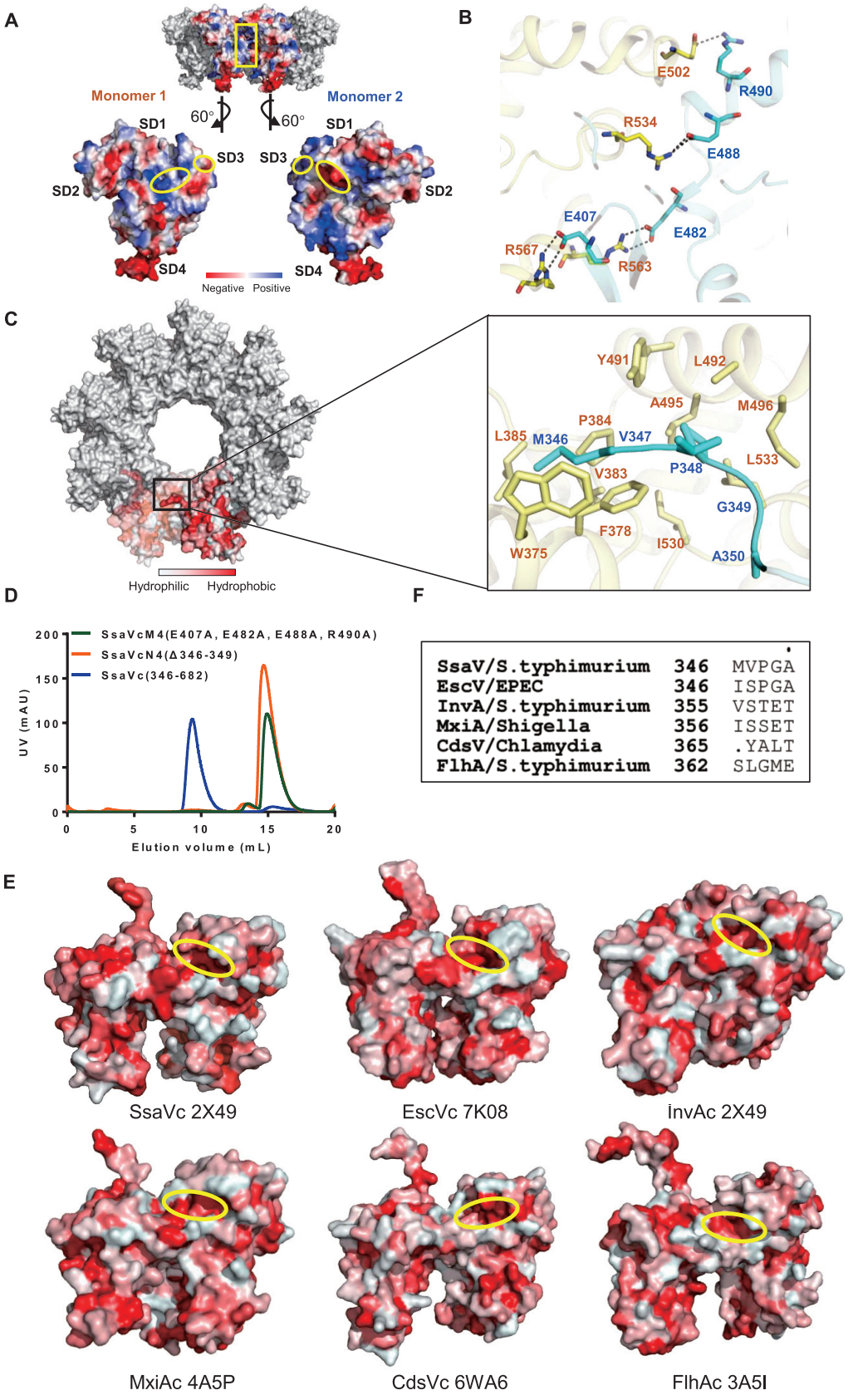

FIG 4 The linker region is important for assembly of the $SsaV_C$ nonameric ring. (A) The electrostatic surface between two adjacent monomers of $SsaV_C$. The complementary electrostatic interactions in SD1-SD3 are highlighted by yellow

(Continued on next page)

different strengths of intermolecular hydrophobic interactions provide possible explanations for why $InvA_C$ is unable to form the nonameric ring in solution (Fig. 1B and C) and why the ring structures of $EscV_C$ and $FlhA_C$ are disassembled in high-concentration salt buffer (32, 45). The relatively strong hydrophobic interactions via the unique amino acid sequence of $SsaV_L$ and the conserved salt bridges between adjacent subunits of $SsaV_C$ can promote formation of a high-order oligomer in different conditions, which may evolve to adapt to the unique environment of the SCV.

The SsaV linker region in chimeric ISS exhibits variable conformations. The structural and functional analysis above shows that the peptide between $SsaV_L$ and $SsaV_C$ plays an essential role in stabilizing the SsaV ring structure. The structural features of TM and linker regions of SctV were previously shown only using *in situ* cryo-ET method (12). To review more structural information of $SsaV_L$ and $InvA_{TM}$, we further processed the cryo-EM data of the chimeric ISS in two independent strategies (Fig. S7 in the supplemental material) via which linker conformational changes of SctV were observed.

In the side views of 2D classification, clear features of the $SsaV_L$ region were captured between the $SsaV_C$ ring structure and the blurry micelle of InvA TM domain (Fig. 5A). A characteristic class of ISS map featured with visible TM region and linker region (highlighted in the red box) was obtained from 3D classifications (details in Materials and Methods and Fig. S7). Using 3D classification with this map as the reference without a local mask, the linker region was classified into variable conformations, with two major orientations, featured as left and right linkers (Fig. 5B, bottom-left panel). For independent validation of variable states of the linker region, a 3D classification was performed by skipping alignment with a local mask in the linker region, and classes of the linker region in different orientations (left and right linker) were obtained (Fig. 5B, bottom-right panel). The linker region obtained from the two separate methods both exhibit two major states of $SsaV_L$ with different orientations relative to $SsaV_C$ in the fixed position (Fig. 5C and Fig. S7). The distance between $InvA_{TM}$ and $SsaV_C$ appears to vary in these two conformations at current resolution (Fig. 5C). The intriguing conformational changes of $SsaV_L$ implies that SsaV might undergo a dynamic process during the substrate selection and secretion. However, more comprehensive and accurate information on the functional mechanism of SctV will require high-resolution SctV full-length structures in different conformations.

DISCUSSION

As one of the engines of T3SS, SctV plays essential roles in effector selection and secretion. Due to the challenges in obtaining well-assembled SctV outside of the bacterial inner membrane, the structure and functional mechanism of SctV have been largely undefined. Through constructing the $InvA_{TM}$-$SsaV_C$ chimeric protein, we produced a homogenous high-order oligomeric SctV protein for cryo-EM structural study. However, we could only determine the high-resolution structure of nonameric $SsaV_C$ and show a low-resolution map of $SsaV_L$. A few of features of $InvA_{TM}$ can also be observed (Fig. 5C and Fig. S7) but detailed structural information was lacked even after intense data processing. It might be resulted from the high flexibility of linker region, otherwise, $InvA_{TM}$ might be intrinsically unstable or even unable to form the nonamer

FIG 4 Legend (Continued)

circles. (B) Cartoon of the interface between two adjacent monomers, showing intermolecular salt-bridges residues as sticks: E407-R567, R563-E482, R534-E488, E502-R490. (C) Analysis of hydrophobic interaction between two adjacent monomers. The cartoon presentation of the hydrophobic interactions is shown enlarged in the right panel. A hydrophobic peptide (346-350) shown as sticks from the linker region (cyan) is nestled into a hydrophobic pocket in the neighboring monomer (yellow). These residues in the hydrophobic pocket with their side chains are shown as sticks. (D) Gel filtration traces of purified $SsaV_C$, $SsaV_C$N4(Δ346-349), and $SsaV_C$M4(E407A, E482A, E488A, R490A). $SsaV_C$N4, with a deletion of the hydrophobic peptide (residues 346–349) and $SsaV_C$M4, with mutations in the salt-bridges, cannot form a nonameric ring. (E) Surface hydrophobic analysis in different homologous proteins. The similar locations of the hydrophobic pockets described in C are highlighted with yellow circles in these proteins. (F) Sequence alignment of the hydrophobic peptides from the linker region in different homologous proteins with solved structures. These residues appear to have different properties, with the hydrophobicity in SsaV stronger than in others.

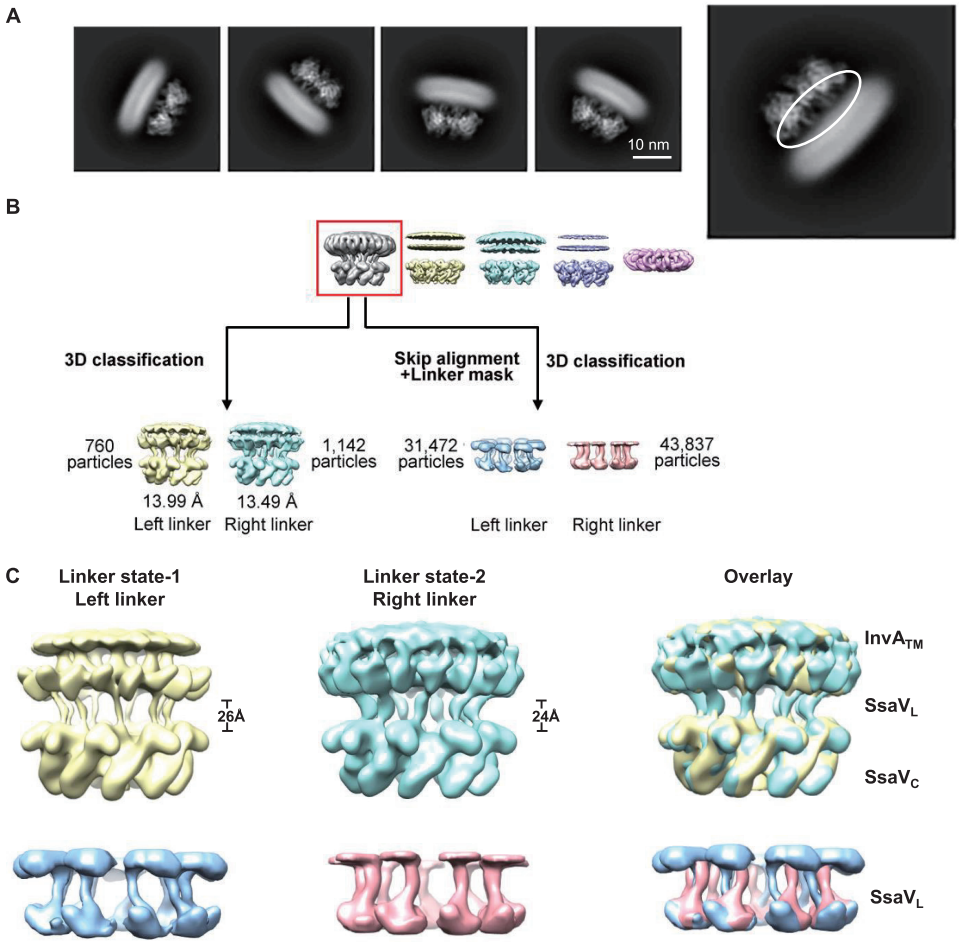

FIG 5 The linker region of the ISS exhibits variable conformations. (A) Representative 2D class averages of the chimeric ISS full-length protein. The linker region is clearly visible and highlighted with a white circle in the right panel. (B) Brief flowchart of EM data processing for the ISS linker region. A characteristic class featured with visible TM region and linker region (highlighted in red box) was obtained from 3D classifications (details in Materials and Methods and Fig. S7). Using 3D classification with this map as reference, the linker region was classified into variable conformations, with two major orientations, named left and right linkers (bottom-left panel). For independent validation of variable states of the linker region, a 3D classification by skipping alignment with a local mask in the linker region was performed and classes of the linker region in different orientations (left and right linker) were obtained (bottom-right panel). (C) Structural comparisons for linker regions of the ISS maps. Structural presentation and overlay comparison for left (colored in yellow) and right linker (colored in cyan) in whole maps of the ISS (top panel). Structural presentation and overlay comparison for left (colored in marine) and right linker (colored in pink) in maps of the ISS with a local mask in the linker regions (bottom panel). Notably, a few of features of TM region can be seen in the whole maps of the ISS.

when it is extracted from the bacterial membrane, perhaps resulting from losing structural support from other partners of the T3SS. Further efforts may be needed to reconstitute SctV into the lipid membrane, perhaps with other potential interaction partners, to force $SctV_{TM}$ to form the stable nonamer.

It has been hypothesized that T3SS is energized by the ATPase-dependent ATP hydrolysis coupled with the proton-motive force (PMF) to secrete unfolded effectors, which is executed by the complex of export gate protein (SctV), center stalk protein (SctO), and ATPase (SctN) with a rotary catalytic mechanism on ATP hydrolysis consistent with the evolutionarily related F_0F_1-ATPase (25–28, 56–60). In F_0F_1-ATPase, the membrane-embedded c ring of F_0 and hydrophilic ATPase F_1 are two rotatory motors connected via the γ-subunit to translocate protons and generate a difference in potential by hydrolyzing ATP (56, 60). However, how the PMF and ATP hydrolysis coupling for the substrate secretion of T3SS is largely unknown. In our study, the 3D classification of $SsaV_L$ shows two major orientations of $SsaV_L$, implying that $SsaV_L$ could be very

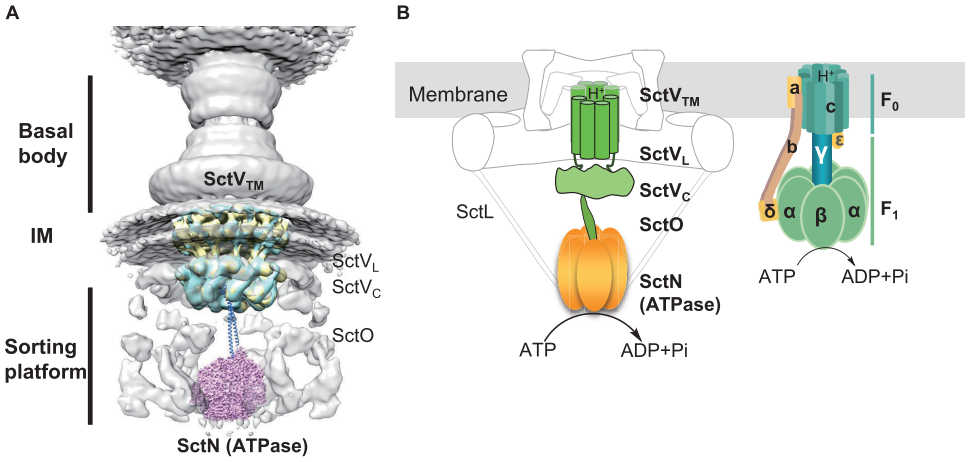

FIG 6 Model for putative mechanism in SctV coupling with ATPase complex. (A) Overview of the location of SctVON complex in the context of the *Salmonella* T3SS injectisome. SctV with two major states and the central stalk protein SctO (CdsO, marine) and the ATPase SctN (EscN, purple, PDB 6NJP) were docked into cryo-ET map of *Salmonella* Type III secretion injectisome map (EMD-8544). The CdsO structure was obtained by Phyre2 based on homology with YscO (PDB 4MH6). (B) Constructional, compositional and functional similarity between T3SS core engine system SctVON complex and F_0F_1-ATPase. Schematic diagrams of T3SS SctVON complex (left panel) and F_0F_1-ATPase (right panel). In F_0F_1-ATPase, the membrane-embedded c ring of F_0 and hydrophilic ATPase F_1 are two rotatory motors connected via the γ-subunit to translocate protons and generate a difference in potential by hydrolyzing ATP. In T3SS, the ATPase complex (SctN) is associated with the export gate (SctV) through interaction with the central stalk (SctO). The ATPase complex (SctN) generates energy by ATP hydrolysis in a rotary catalytic mechanism, which may drive effectors unfolding and secretion coupling with PMF generated by SctV in a cooperative manner.

dynamic during its functioning. The dynamic $SctV_L$, $SctV_C$, and SctO might form a bridge to coordinate the coupling between the $SctV_{TM}$ (PMF) and SctN (ATP hydrolysis) to facilitate the substrate secretion of T3SS in an efficient manner (Fig. 6A). The dynamic conformation of $SctV_L$ may also provide a structural explanation for the resent model for the action of FlhA in flagellar export that the $FlhA_C$/$SctV_C$ need to move to the $FlhA_{TM}$/$SctV_{TM}$ back and forth during the secretion cycle (49). Furthermore, considering the constructional, compositional and functional similarity between T3SS core engine system (SctVON) and F_0F_1-ATPase (Fig. 6B), as well as our observation of highly dynamic loop region of SctV in the full-length context, suggests an interesting hypothesis that T3SS may share a conserved rotary catalytic mechanism (SctV and SctN as two rotatory motors coupled via the SctO) with F_0F_1-ATPase to generate energy for protein secretion. However, this rotating model during SctV functioning is highly speculative. Further high-resolution full-length SctV structures and functional assays are imperative to fully dissect the molecular mechanism of how T3SS is energized for protein selection and secretion.

$SctV_C$ was reported to involve substrate selection and secretion through the intramolecular cleft formed by SD2 and SD4 and the intermolecular cleft formed by two neighboring SD4s (13, 32). The SD2-SD4 cleft is dynamic and ranges from open to closed to selectively bind and release effector-chaperon pairs (13). The SD4-SD4 cleft has been shown to interact with central stalk protein SctO to facilitate the connection between SctV and ATPase SctN (26, 61). Due to the essential function of SctV in the T3SS secretion process, blockage of these two vital clefts of SctV should significantly diminish the function of T3SS and the virulence of the T3SS-employing bacterial pathogens (59). Therefore, $SctV_C$ could be considered a potential novel target for developing anti-virulence drugs to some antibiotic resistant Gram-negative bacterial pathogens.

In this paper, we present near atomic-level insights into the assembly and functional mechanism of $SctV_C$ and report variable states of SctV linker region. This study sheds light on important but heretofore poorly understood aspects of the remarkably complex biology of T3SS export gate protein SctV and thus has important implications

for the development of therapeutic strategies targeting $SctV_C$ to combat T3SS-mediated bacterial infection.

MATERIALS AND METHODS

Expression and purification of $SsaV_C$ and $InvA_{TM}$-$SsaV_C$ chimera. The DNA for $SsaV_C$ (encoding residues 346–682) was cloned into pET15b (Novagen, Gibbstown, NJ) with a thrombin-cleavable His_6 tag at the N-terminus. To generate the $InvA_{TM}$-$SsaV_C$ chimera, residues 316–685 of InvA were replaced by residues 326–682 of SsaV through Gibson assembly (62). All primers used in this study are listed in Table S2 in the supplemental material and all constructs were checked by DNA sequencing. An N-terminal Strep-tag and a SUMO protein in tandem were fused with $InvA_{TM}$-$SsaV_C$ chimera. Overexpression in *Escherichia coli* BL21 was induced overnight with 0.2 mM isopropyl-β-d-thiogalactopyranoside (IPTG) at 22°C when OD_{600} reached 0.8 (for $InvA_{TM}$-$SsaV_C$ chimera, OD_{600} = 1.2).

For purification of $SsaV_C$, culture was harvested by centrifugation at 5,050 $\times$ *g* for 15 min at 4 °C and resuspended in lysis buffer containing 20 mM Tris-HCl (pH 8.0) and 150 mM NaCl and disrupted through a high-pressure homogenizer. After centrifugation at 17,000 $\times$ *g* for 50 min at 4 °C, the supernatant was applied into Ni-NTA resin (Qiagen, Hilden, Germany) and washed three times with 10 ml lysis buffer plus 20 mM imidazole. The protein was then eluted with lysis buffer with 300 mM imidazole, and further purified through an anion-exchange column (Hitrap Q, GE Healthcare, Fairfield, CT). Peak fractions were pooled and concentrated using 10 kDa cutoff Centricon filters (Millipore, Boston, MA) and subjected to size exclusion chromatography (Superdex 200 Increase 10/300 GL, GE Healthcare) in the lysis buffer. Finally, peak fractions were collected and concentrated to 5 mg/ml by 100 kDa cutoff Centricon filters for cryo-EM analysis.

To purify the $InvA_{TM}$-$SsaV_C$ chimera protein, 6 L of culture was collected, resuspended in lysis buffer, and disrupted through a high-pressure homogenizer. Insoluble fractions were removed by centrifugation at 20,000 $\times$ *g* for 20 min, while the supernatant was further ultracentrifuged at 150,000 $\times$ *g* for 1 h. The pellet (containing the membrane fraction) was resuspended in lysis buffer supplemented with 1% (wt/vol%) GDN and incubated at 4°C overnight. After centrifugation at 150,000 $\times$ *g* for 30 min, the supernatant was applied into Strep-Tactin Beads (Smart-Lifesciences, Changzhou, China) by gravity and washed with buffer W (lysis buffer plus 0.004% [wt/vol%] GDN). The target protein was eluted with buffer W after the SUMO tag was cleaved on the beads. The eluent was concentrated with a 100 kDa cutoff Centricon filter and further purified through size exclusion chromatography (Superose 6 Increase, GE Healthcare) in buffer W. SsaV and InvA were purified using the same procedure. For detergent screening, detergents were changed from membrane extraction to Superose 6 column in the purification. For cryo-EM analysis, peak fractions were concentrated to ~10 mg/ml using 100 kDa cutoff Centricon filters.

Cryo-EM data acquisition. Aliquots of 4 μl concentrated samples were applied to glow-discharged holey carbon-coated grids (Quantifoil Au R1.2/1.3, 200 mesh, Beijing Zhongjingkeyi Technology, Beijing, China). Grids were blotted for 3.5 s at 8 °C with 100% humidity and frozen in liquid ethane using a Vitrobot Mark IV (Thermo Fisher Scientific, Waltham, MA). Grids were transferred to a Titan Krios (Thermo Fisher Scientific) operating at 300 kV and equipped with Gatan K3 Summit detector (Pleasanton, CA) and a GIF Quantum energy filter (slit width 20 eV). Micrographs were recorded in the super-resolution mode with a nominal magnification of 105,000x, resulting in a calibrated pixel size of 0.422 Å. Each stack of 32 frames was exposed for 2.13 s with an exposing time of 0.067 s per frame. The total dose was ~ 50 e-/Å^2 for each stack. AutoEMation (63) was used for the fully automated data collection. All 32 frames in each stack were aligned and summed using the whole-image motion correction program MotionCor2 (64) and binned to a pixel size of 0.8433 Å. The defocus value of each image was set to -0.8 μm to -1.5 μm and determined in cryoSPARC (65).

EM data processing for $SsaV_C$. The data acquisition of $SsaV_C$ is described as above Cryo-EM data acquisition section (named as data set 1). Out of 4,020 micrographs, 1,987,239 particles were automatically picked by cryoSPARC. After two rounds of 2D classification using cryoSPARC, a small subset of good particles was selected to generate the initial model; 584,301 good particles after 2D classification were used for 3D classification with C9 symmetry using cryoSPARC. Double-layer class (111,741 particles) and single-layer class (90,916 particles) were classified and further processed using Non-Uniform refinement, with D9 and C9 symmetry, respectively, resulting in double-layer map at 3.55 Å and single-layer map at 3.64 Å. A flowchart showing the data processing is shown in Fig. S1 in the supplemental material.

EM data processing for $InvA_{TM}$-$SsaV_C$ chimeric protein (ISS). (i) Data processing for $SsaV_C$ of ISS. The data acquisition of chimeric ISS is described as above Cryo-EM data acquisition section (named as data set 2). Out of 11,550 micrographs, 3,673,478 particles were automatically picked by cryoSPARC. After two rounds of 2D classification using cryoSPARC, a small subset of good particles was selected to generate the initial model: 1,225,081 good particles after 2D classification were used for 3D classification with C9 symmetry using cryoSPARC, and 734,284 good particles from the 3D classification were processed with further nonuniform refinement and local CTF refinement with C9 symmetry, resulting in the $SsaV_C$ EM map with an averaged resolution at 2.11 Å. Features of the TM region and linker region of ISS are invisible in this map at current resolution. A flowchart showing the data processing is shown in Fig. S2 in the supplemental material.

(ii) Data processing for Initial model of $InvA_{TM}$. For checking the sample quality of the $InvA_{TM}$-$SsaV_C$ chimeric protein, 168 micrograph stacks were recorded using Talos Arctica (Thermo Fisher Scientific) at 200 kV equipped with a K2 detector (Pleasanton, CA), with motion correction using with MotionCor2 and CTF estimation using cryoSPARC, resulting in a calibrated pixel size of 1.17 Å. Out of 168 micrographs, 52,849 particles were automatically picked by cryoSPARC. After two rounds of 2D classification

using RELION3.0 (66), a small subset of good particles was selected to generate the initial model; 44,442 good particles after 2D classification were used for 3D classification with C9 symmetry using RELION3.0. A representative $InvA_{TM}$ map with featured TM region was obtained from 3D classification (Fig. S7A, red box, Model 1, 14,370 particles). A flowchart showing the data processing is shown in Fig. S7A.

(iii) Data processing for $InvA_{TM}$ and $SsaV_L$ without local mask. For the $InvA_{TM}$-$SsaV_C$ chimeric protein described as above (data set 2), 375,338 particles in side views after 2D classifications were selected to process with 3D classification using Model 1 obtained above as the reference with C9 symmetry using RELION3.0, resulting in a full-length EM map class of $InvA_{TM}$-$SsaV_C$ chimeric protein with features of $InvA_{TM}$, $SsaV_L$, and $SsaV_C$ (Fig. S7B, red box, Model 2, 28,922 particles). After two rounds of 3D classification, ISS EM maps with different linker states (Left', Left, Right, Right') were obtained. Representative EM maps (Left linker, 13.99 Å and Right linker, 13.49 Å) were obtained after refinement using RELION3.0. Reported resolutions were calculated on the basis of the FSC 0.143 criterion. A flowchart showing the data processing is shown in Fig. S7B in the supplemental material.

(iv) Data processing for $SsaV_L$ with local mask. For further estimating linker states of SsaV, 546,372 particles after 2D classification described above (Data set 2) were used to run a 3D classification by skipping alignment, using Model 2 as the reference, with a local mask in the linker region and C9 symmetry using RELION3.0. Two distinguished classes featured with left linker (31,427 particles) and right linker (43,387 particles) were obtained from the 3D classification. A flowchart showing the data processing is shown in Fig. S7C in the supplemental material.

Model building and structure refinement. The 2.11 Å reconstruction map was used for model building. The starting model of $SsaV_C$ based on the structure of $SsaV_C$ (PDB:7AWA) was manually built in Coot (67), followed by refinement against the corresponding maps in PHENIX (68) with secondary structure and geometry restraints. Statistics of 3D reconstruction and model refinement are summarized in Table S1 in the supplemental material. Structural figures were made using PyMOL v.2.3.2 (69) and UCSF ChimeraX v.1.1 (70). Analysis of sequence conservation was determined by the ConSurf server (71) according to sequence alignment using ClustalW (72). The pore diameter diagram calculated using the Hole program (73) in Coot. Phyre2 (74) was used to model the protein structures.

DLS measurement. DLS measurements were carried out using cuvette-based systems on a DynaPro NanoStar (WYATT, Santa Barbara, CA). Purified proteins were diluted to 0.5 mg/ml in lysis buffer containing 20 mM Tris-HCl (pH 8.0) and 150 mM NaCl. After centrifugation at 17,000 $\times$ *g* for 5 min, aliquots of 8 μl of samples were analyzed at 25 °C.

SUPPLEMENTAL MATERIAL

Supplemental material is available online only.

SUPPLEMENTAL FILE 1, PDF file, 1.7 MB.

ACKNOWLEDGMENTS

We thank Jorge Galan (Yale University) and Yongjian Huang (University of California, Berkeley) for constructive and helpful discussions and Yigong Shi (Westlake University) for his kind support on cryo-EM resource and computational resource during this project. We thank Xiaoju Li from Core facilities for life and environmental sciences, Shandong University and Kang Li from the cryo-EM facility for Marine Biology at QNLM for helping with cryo-EM sample screening. We thank Fan Yang (Tsinghua University) for technical support during EM image acquisition. We thank the Tsinghua University Branch of China National Center for Protein Sciences (Beijing) and Fudan University for providing the cryo-EM facility support. We thank the computational facility support on the cluster of Bio-Computing Platform (Tsinghua University Branch of China National Center for Protein Sciences Beijing), Center of Cryo-Electron Microscopy (Fudan University), and HPC Cloud Platform (Shandong University).

The atomic coordinates and EM map have been deposited in the Protein Data Bank (www.rcsb.org) and Electron Microscopy Data Bank (www.ebi.ac.uk/pdbe/emdb/) with the accession codes 7FEB,7FEC,7FED and EMD-31551, EMD-31552, EMD-31553, respectively. Materials are available from the corresponding authors on request.

X.G. and Y.Z. conceived the project. X.G., J.X., and Y.Z. designed the experiment. J.X. performed the experiments of purification with the help of J.W. and all assays. Y.Z. and J.X. performed cryo-EM sample preparation and data collection. Y.Z. performed cryo-EM data processing. J.X. performed structural model building. All authors contributed to data analysis. X.G., Y.Z., and J.X. wrote the manuscript.

This work was funded by the National Key R&D Program of China (2018YFE0113000 to X.G.), National Natural Science Foundation of China (31770143 and 32122007 to X.G.), the Major Basic Program of Natural Science Foundation of Shandong Province (ZR2019ZD21 to X.G.), the Youth Interdisciplinary Innovative Research Group of

Shandong University (2020QNQT009 to X.G.), the Taishan Young Scholars Program (tsqn20161005 to X.G.), Shanghai Rising-Star Program (21QA1401200 to Y.Z.), Original Research Program from Fudan University (IDH1340064/009 to Y.Z.), and startup funds from Fudan University (JIH1340063 to Y.Z.).

We declare that the research was conducted in the absence of any commercial or financial relationships that could be construed as a potential conflict of interest.

REFERENCES

1. Galan JE, Wolf-Watz H. 2006. Protein delivery into eukaryotic cells by type III secretion machines. Nature 444:567–573. https://doi.org/10.1038/nature05272.
2. Hu J, Worrall LJ, Strynadka NC. 2020. Towards capture of dynamic assembly and action of the T3SS at near atomic resolution. Curr Opin Struct Biol 61:71–78. https://doi.org/10.1016/j.sbi.2019.10.005.
3. Diepold A, Armitage JP. 2015. Type III secretion systems: the bacterial flagellum and the injectisome. Philos Trans R Soc Lond B Biol Sci 370. https://doi.org/10.1098/rstb.2015.0020.
4. Deng W, Marshall NC, Rowland JL, McCoy JM, Worrall LJ, Santos AS, Strynadka NCJ, Finlay BB. 2017. Assembly, structure, function and regulation of type III secretion systems. Nat Rev Microbiol 15:323–337. https://doi.org/10.1038/nrmicro.2017.20.
5. Erhardt M, Namba K, Hughes KT. 2010. Bacterial nanomachines: the flagellum and type III injectisome. Cold Spring Harb Perspect Biol 2:a000299. https://doi.org/10.1101/cshperspect.a000299.
6. Armitage JP, Berry RM. 2020. Assembly and dynamics of the bacterial flagellum. Annu Rev Microbiol 74:181–200. https://doi.org/10.1146/annurev-micro-090816-093411.
7. Galan JE, Lara-Tejero M, Marlovits TC, Wagner S. 2014. Bacterial type III secretion systems: specialized nanomachines for protein delivery into target cells. Annu Rev Microbiol 68:415–438. https://doi.org/10.1146/annurev-micro-092412-155725.
8. Shenoy AR, Furniss RCD, Goddard PJ, Clements A. 2018. Modulation of host cell processes by T3SS effectors. Curr Top Microbiol Immunol 416:73–115. https://doi.org/10.1007/82_2018_106.
9. Nans A, Kudryashev M, Saibil HR, Hayward RD. 2015. Structure of a bacterial type III secretion system in contact with a host membrane in situ. Nat Commun 6:10114. https://doi.org/10.1038/ncomms10114.
10. Lara-Tejero M, Kato J, Wagner S, Liu X, Galan JE. 2011. A sorting platform determines the order of protein secretion in bacterial type III systems. Science 331:1188–1191. https://doi.org/10.1126/science.1201476.
11. Schraidt O, Marlovits TC. 2011. Three-dimensional model of salmonella's needle complex at subnanometer resolution. Science 331:1192–1195. https://doi.org/10.1126/science.1199358.
12. Butan C, Lara-Tejero M, Li W, Liu J, Galan JE. 2019. High-resolution view of the type III secretion export apparatus in situ reveals membrane remodeling and a secretion pathway. Proc Natl Acad Sci U S A 116:24786–24795. https://doi.org/10.1073/pnas.1916331116.
13. Inoue Y, Ogawa Y, Kinoshita M, Terahara N, Shimada M, Kodera N, Ando T, Namba K, Kitao A, Imada K, Minamino T. 2019. Structural insights into the substrate specificity switch mechanism of the type III protein export apparatus. Structure 27:965–976. https://doi.org/10.1016/j.str.2019.03.017.
14. Zhang Y, Lara-Tejero M, Bewersdorf J, Galan JE. 2017. Visualization and characterization of individual type III protein secretion machines in live bacteria. Proc Natl Acad Sci U S A 114:6098–6103. https://doi.org/10.1073/pnas.1705823114.
15. Yu XJ, McGourty K, Liu M, Unsworth KE, Holden DW. 2010. pH sensing by intracellular Salmonella induces effector translocation. Science 328:1040–1043. https://doi.org/10.1126/science.1189000.
16. Johnson R, Mylona E, Frankel G. 2018. Typhoidal salmonella: Distinctive virulence factors and pathogenesis. Cell Microbiol 20:e12939. https://doi.org/10.1111/cmi.12939.
17. Lou L, Zhang P, Piao R, Wang Y. 2019. Salmonella pathogenicity island 1 (SPI-1) and its complex regulatory network. Front Cell Infect Microbiol 9:270. https://doi.org/10.3389/fcimb.2019.00270.
18. Que F, Wu S, Huang R. 2013. Salmonella pathogenicity island 1(SPI-1) at work. Curr Microbiol 66:582–587. https://doi.org/10.1007/s00284-013-0307-8.
19. Knodler LA, Celli J, Hardt WD, Vallance BA, Yip C, Finlay BB. 2002. Salmonella effectors within a single pathogenicity island are differentially expressed and translocated by separate type III secretion systems. Mol Microbiol 43:1089–1103. https://doi.org/10.1046/j.1365-2958.2002.02820.x.
20. Waterman SR, Holden DW. 2003. Functions and effectors of the Salmonella pathogenicity island 2 type III secretion system. Cell Microbiol 5:501–511. https://doi.org/10.1046/j.1462-5822.2003.00294.x.
21. Jennings E, Thurston TLM, Holden DW. 2017. Salmonella SPI-2 type III secretion system effectors: Molecular mechanisms and physiological consequences. Cell Host Microbe 22:217–231. https://doi.org/10.1016/j.chom.2017.07.009.
22. Chakravortty D, Rohde M, Jager L, Deiwick J, Hensel M. 2005. Formation of a novel surface structure encoded by Salmonella Pathogenicity Island 2. EMBO J 24:2043–2052. https://doi.org/10.1038/sj.emboj.7600676.
23. Laughlin RC, Knodler LA, Barhoumi R, Payne HR, Wu J, Gomez G, Pugh R, Lawhon SD, Baumler AJ, Steele-Mortimer O, Adams LG. 2014. Spatial segregation of virulence gene expression during acute enteric infection with Salmonella enterica serovar Typhimurium. mBio 5:e00946-13–e00913. https://doi.org/10.1128/mBio.00946-13.
24. Galan JE, Ginocchio C, Costeas P. 1992. Molecular and functional characterization of the Salmonella invasion gene invA: Homology of InvA to members of a new protein family. J Bacteriol 174:4338–4349. https://doi.org/10.1128/jb.174.13.4338-4349.1992.
25. Lee PC, Rietsch A. 2015. Fueling type III secretion. Trends Microbiol 23:296–300. https://doi.org/10.1016/j.tim.2015.01.012.
26. Jensen JL, Yamini S, Rietsch A, Spiller BW. 2020. The structure of the type III secretion system export gate with CdsO, an ATPase lever arm. PLoS Pathog 16:e1008923. https://doi.org/10.1371/journal.ppat.1008923.
27. Nakamura S, Minamino T. 2019. Flagella-driven motility of bacteria. Biomolecules 9:279. https://doi.org/10.3390/biom9070279.
28. Majewski DD, Worrall LJ, Hong C, Atkinson CE, Vuckovic M, Watanabe N, Yu Z, Strynadka NCJ. 2019. Cryo-EM structure of the homohexameric T3SS ATPase-central stalk complex reveals rotary ATPase-like asymmetry. Nat Commun 10:626. https://doi.org/10.1038/s41467-019-08477-7.
29. Minamino T, Morimoto YV, Hara N, Namba K. 2011. An energy transduction mechanism used in bacterial flagellar type III protein export. Nat Commun 2:475. https://doi.org/10.1038/ncomms1488.
30. Yu XJ, Liu M, Holden DW. 2004. SsaM and SpiC interact and regulate secretion of Salmonella pathogenicity island 2 type III secretion system effectors and translocators. Mol Microbiol 54:604–619. https://doi.org/10.1111/j.1365-2958.2004.04297.x.
31. Kim JS, Jang JI, Eom JS, Oh CH, Kim HG, Kim BH, Bang IS, Bang SH, Park YK. 2013. Molecular characterization of the InvE regulator in the secretion of type III secretion translocases in Salmonella enterica serovar Typhimurium. Microbiology (Reading) 159:446–461. https://doi.org/10.1099/mic.0.061689-0.
32. Xing Q, Shi K, Portaliou A, Rossi P, Economou A, Kalodimos CG. 2018. Structures of chaperone-substrate complexes docked onto the export gate in a type III secretion system. Nat Commun 9:1773. https://doi.org/10.1038/s41467-018-04137-4.
33. Archuleta TL, Spiller BW. 2014. A gatekeeper chaperone complex directs translocator secretion during type three secretion. PLoS Pathog 10:e1004498. https://doi.org/10.1371/journal.ppat.1004498.
34. Gaytan MO, Monjaras Feria J, Soto E, Espinosa N, Benitez JM, Georgellis D, Gonzalez-Pedrajo B. 2018. Novel insights into the mechanism of SepL-mediated control of effector secretion in enteropathogenic Escherichia coli. Microbiologyopen 7:e00571. https://doi.org/10.1002/mbo3.571.
35. Ginocchio CC, Galan JE. 1995. Functional conservation among members of the Salmonella typhimurium InvA family of proteins. Infect Immun 63:729–732. https://doi.org/10.1128/iai.63.2.729-732.1995.
36. Marlovits TC, Kubori T, Sukhan A, Thomas DR, Galan JE, Unger VM. 2004. Structural insights into the assembly of the type III secretion needle complex. Science 306:1040–1042. https://doi.org/10.1126/science.1102610.
37. Burkinshaw BJ, Strynadka NC. 2014. Assembly and structure of the T3SS. Biochim Biophys Acta 1843:1649–1663. https://doi.org/10.1016/j.bbamcr.2014.01.035.

38. Hu B, Morado DR, Margolin W, Rohde JR, Arizmendi O, Picking WL, Picking WD, Liu J. 2015. Visualization of the type III secretion sorting platform of Shigella flexneri. Proc Natl Acad Sci U S A 112:1047–1052. https://doi.org/10.1073/pnas.1411610112.
39. Hu B, Lara-Tejero M, Kong Q, Galan JE, Liu J. 2017. In situ molecular architecture of the salmonella type III secretion machine. Cell 168:1065–1074. https://doi.org/10.1016/j.cell.2017.02.022.
40. Hu J, Worrall LJ, Hong C, Vuckovic M, Atkinson CE, Caveney N, Yu Z, Strynadka NCJ. 2018. Cryo-EM analysis of the T3S injectisome reveals the structure of the needle and open secretin. Nat Commun 9:3840. https://doi.org/10.1038/s41467-018-06298-8.
41. Tan J, Zhang X, Wang X, Xu C, Chang S, Wu H, Wang T, Liang H, Gao H, Zhou Y, Zhu Y. 2021. Structural basis of assembly and torque transmission of the bacterial flagellar motor. Cell 184:2665–2679. https://doi.org/10.1016/j.cell.2021.03.057.
42. Johnson S, Furlong EJ, Deme JC, Nord AL, Caesar JJE, Chevance FFV, Berry RM, Hughes KT, Lea SM. 2021. Molecular structure of the intact bacterial flagellar basal body. Nat Microbiol 6:712–721. https://doi.org/10.1038/s41564-021-00895-y.
43. Wagner S, Konigsmaier L, Lara-Tejero M, Lefebre M, Marlovits TC, Galan JE. 2010. Organization and coordinated assembly of the type III secretion export apparatus. Proc Natl Acad Sci U S A 107:17745–17750. https://doi.org/10.1073/pnas.1008053107.
44. Abrusci P, Vergara-Irigaray M, Johnson S, Beeby MD, Hendrixson DR, Roversi P, Friede ME, Deane JE, Jensen GJ, Tang CM, Lea SM. 2013. Architecture of the major component of the type III secretion system export apparatus. Nat Struct Mol Biol 20:99–104. https://doi.org/10.1038/nsmb.2452.
45. Majewski DD, Lyons BJE, Atkinson CE, Strynadka NCJ. 2020. Cryo-EM analysis of the SctV cytosolic domain from the enteropathogenic E. coli T3SS injectisome. J Struct Biol 212:107660. https://doi.org/10.1016/j.jsb.2020.107660.
46. Yuan B, Portaliou AG, Parakra R, Smit JH, Wald J, Li Y, Srinivasu B, Loos MS, Dhupar HS, Fahrenkamp D, Kalodimos CG, Duong van Hoa F, Cordes T, Karamanou S, Marlovits TC, Economou A. 2021. Structural dynamics of the functional nonameric type III translocase export gate. J Mol Biol 433:167188. https://doi.org/10.1016/j.jmb.2021.167188.
47. Matthews-Palmer TRS, Gonzalez-Rodriguez N, Calcraft T, Lagercrantz S, Zachs T, Yu XJ, Grabe GJ, Holden DW, Nans A, Rosenthal PB, Rouse SL, Beeby M. 2021. Structure of the cytoplasmic domain of SctV (SsaV) from the Salmonella SPI-2 injectisome and implications for a pH sensing mechanism. J Struct Biol 213:107729. https://doi.org/10.1016/j.jsb.2021.107729.
48. Kuhlen L, Johnson S, Cao J, Deme JC, Lea SM. 2021. Nonameric structures of the cytoplasmic domain of FlhA and SctV in the context of the full-length protein. PLoS One 16:e0252800. https://doi.org/10.1371/journal.pone.0252800.
49. Erhardt M, Wheatley P, Kim EA, Hirano T, Zhang Y, Sarkar MK, Hughes KT, Blair DF. 2017. Mechanism of type-III protein secretion: Regulation of FlhA conformation by a functionally critical charged-residue cluster. Mol Microbiol 104:234–249. https://doi.org/10.1111/mmi.13623.
50. Terahara N, Inoue Y, Kodera N, Morimoto YV, Uchihashi T, Imada K, Ando T, Namba K, Minamino T. 2018. Insight into structural remodeling of the FlhA ring responsible for bacterial flagellar type III protein export. Sci Adv 4:eaao7054. https://doi.org/10.1126/sciadv.aao7054.
51. Worrall LJ, Vuckovic M, Strynadka NC. 2010. Crystal structure of the C-terminal domain of the Salmonella type III secretion system export apparatus protein InvA. Protein Sci 19:1091–1096. https://doi.org/10.1002/pro.382.
52. D'Imprima E, Floris D, Joppe M, Sanchez R, Grininger M, Kuhlbrandt W. 2019. Protein denaturation at the air-water interface and how to prevent it. Elife 8. https://doi.org/10.7554/eLife.42747.
53. Minamino T. 2018. Hierarchical protein export mechanism of the bacterial flagellar type III protein export apparatus. FEMS Microbiol Lett 365. https://doi.org/10.1093/femsle/fny117.
54. Radics J, Konigsmaier L, Marlovits TC. 2014. Structure of a pathogenic type 3 secretion system in action. Nat Struct Mol Biol 21:82–87. https://doi.org/10.1038/nsmb.2722.
55. Saijo-Hamano Y, Imada K, Minamino T, Kihara M, Shimada M, Kitao A, Namba K. 2010. Structure of the cytoplasmic domain of FlhA and implication for flagellar type III protein export. Mol Microbiol 76:260–268. https://doi.org/10.1111/j.1365-2958.2010.07097.x.
56. Murphy BJ, Klusch N, Langer J, Mills DJ, Yildiz O, Kuhlbrandt W. 2019. Rotary substates of mitochondrial ATP synthase reveal the basis of flexible F1-Fo coupling. Science 364:eaaw9128. https://doi.org/10.1126/science.aaw9128.
57. Minamino T, Morimoto YV, Hara N, Aldridge PD, Namba K. 2016. The bacterial flagellar type III export gate complex is a dual fuel engine that can use both H+ and Na+ for flagellar protein export. PLoS Pathog 12:e1005495. https://doi.org/10.1371/journal.ppat.1005495.
58. Ibuki T, Imada K, Minamino T, Kato T, Miyata T, Namba K. 2011. Common architecture of the flagellar type III protein export apparatus and F- and V-type ATPases. Nat Struct Mol Biol 18:277–282. https://doi.org/10.1038/nsmb.1977.
59. Rasko DA, Sperandio V. 2010. Anti-virulence strategies to combat bacteria-mediated disease. Nat Rev Drug Discov 9:117–128. https://doi.org/10.1038/nrd3013.
60. Imada K, Minamino T, Tahara A, Namba K. 2007. Structural similarity between the flagellar type III ATPase FliI and F1-ATPase subunits. Proc Natl Acad Sci U S A 104:485–490. https://doi.org/10.1073/pnas.0608090104.
61. Shen DK, Blocker AJ. 2016. MxiA, MxiC and IpaD regulate substrate selection and secretion mode in the T3SS of Shigella flexneri. PLoS One 11:e0155141. https://doi.org/10.1371/journal.pone.0155141.
62. Gibson DG, Young L, Chuang RY, Venter JC, Hutchison CA, 3rd, Smith HO. 2009. Enzymatic assembly of DNA molecules up to several hundred kilobases. Nat Methods 6:343–345. https://doi.org/10.1038/nmeth.1318.
63. Lei J, Frank J. 2005. Automated acquisition of cryo-electron micrographs for single particle reconstruction on an FEI Tecnai electron microscope. J Struct Biol 150:69–80. https://doi.org/10.1016/j.jsb.2005.01.002.
64. Zheng SQ, Palovcak E, Armache JP, Verba KA, Cheng Y, Agard DA. 2017. MotionCor2: anisotropic correction of beam-induced motion for improved cryo-electron microscopy. Nat Methods 14:331–332. https://doi.org/10.1038/nmeth.4193.
65. Punjani A, Rubinstein JL, Fleet DJ, Brubaker MA. 2017. cryoSPARC: algorithms for rapid unsupervised cryo-EM structure determination. Nat Methods 14:290–296. https://doi.org/10.1038/nmeth.4169.
66. Scheres SH. 2012. RELION: implementation of a Bayesian approach to cryo-EM structure determination. J Struct Biol 180:519–530. https://doi.org/10.1016/j.jsb.2012.09.006.
67. Emsley P, Cowtan K. 2004. Coot: Model-building tools for molecular graphics. Acta Crystallogr D Biol Crystallogr 60:2126–2132. https://doi.org/10.1107/S0907444904019158.
68. Adams PD, Afonine PV, Bunkoczi G, Chen VB, Davis IW, Echols N, Headd JJ, Hung LW, Kapral GJ, Grosse-Kunstleve RW, McCoy AJ, Moriarty NW, Oeffner R, Read RJ, Richardson DC, Richardson JS, Terwilliger TC, Zwart PH. 2010. PHENIX: a comprehensive Python-based system for macromolecular structure solution. Acta Crystallogr D Biol Crystallogr 66:213–221. https://doi.org/10.1107/S0907444909052925.
69. Zhang K. 2016. Gctf: Real-time CTF determination and correction. J Struct Biol 193:1–12. https://doi.org/10.1016/j.jsb.2015.11.003.
70. Pettersen EF, Goddard TD, Huang CC, Couch GS, Greenblatt DM, Meng EC, Ferrin TE. 2004. UCSF Chimera—a visualization system for exploratory research and analysis. J Comput Chem 25:1605–1612. https://doi.org/10.1002/jcc.20084.
71. Landau M, Mayrose I, Rosenberg Y, Glaser F, Martz E, Pupko T, Ben-Tal N. 2005. ConSurf 2005: the projection of evolutionary conservation scores of residues on protein structures. Nucleic Acids Res 33:W299–302. https://doi.org/10.1093/nar/gki370.
72. Sievers F, Wilm A, Dineen D, Gibson TJ, Karplus K, Li W, Lopez R, McWilliam H, Remmert M, Soding J, Thompson JD, Higgins DG. 2011. Fast, scalable generation of high-quality protein multiple sequence alignments using Clustal Omega. Mol Syst Biol 7:539. https://doi.org/10.1038/msb.2011.75.
73. Smart OS, Neduvelil JG, Wang X, Wallace BA, Sansom MS. 1996. HOLE: A program for the analysis of the pore dimensions of ion channel structural models. J Mol Graph 14:354–360. https://doi.org/10.1016/S0263-7855(97)00009-X.
74. Kelley LA, Mezulis S, Yates CM, Wass MN, Sternberg MJ. 2015. The Phyre2 web portal for protein modeling, prediction and analysis. Nat Protoc 10:845–858. https://doi.org/10.1038/nprot.2015.053.